Honeycomb-like Periodic Porous LaFeO₃ Thin Film Chemiresistors with Enhanced Gas-Sensing Performances

Zhengfei Dai, Chul-Soon Lee, Bo-Young Kim, Chang-Hoon Kwak, Ji-Wook Yoon, Hyun-Mook Jeong, and Jong-Heun Lee*

Department of Materials Science and Engineering, Korea University, Seoul 136-713, Republic of Korea

Ⓢ Supporting Information

ABSTRACT: The use of composite materials and polynary compounds is a promising strategy to promote conductometric sensor performances. The perovskite oxides provide various compositional combinations between different oxides for tuning gas-sensing reaction and endowing rich oxygen deficiencies for preferable gas adsorption. Herein, a sacrificial colloidal template approach is exploited to fabricate crystalline ternary LaFeO₃ perovskite porous thin films, by transferring a $La^{3+}-Fe^{3+}$ hybrid solution-dipped template onto a substrate and sequent heat treatment. The honeycomb-like LaFeO₃ film consisted of monolayer periodic pore (size: ~ 500 nm) array can be successfully in situ synthesized in a homogeneous layout with a single phase of perovskite. This periodic porous LaFeO₃ film with p-type semiconductivity exhibits a high gas response, fast response (~4 s), trace detection capacity (50 ppb), and favorable ethanol selectivity from similar acetone. It exhibits enhanced sensing performances compared to those of a binary n-type Fe₂O₃ film and a nontemplated dense LaFeO₃ film. In addition, a five-axe spiderweb diagram is introduced to make a feasible evaluation of the optimal practical work condition, comprehensively regarding the response/recovery rate, gas response, selectivity and operating temperature. The enhanced ethanol sensing mechanism of honeycomb-like LaFeO₃ periodic porous film is also addressed. This novel and facile route to fabricate well-ordered porous LaFeO₃ thin film can also be applied to many fields to obtain special performances, such as solar cells, ion conductors, gas separation, piezoelectricity, and self-powered sensing device system.

KEYWORDS: perovskite structure, semiconducting metal oxides, micro/nanostructure, periodic array, gas sensor
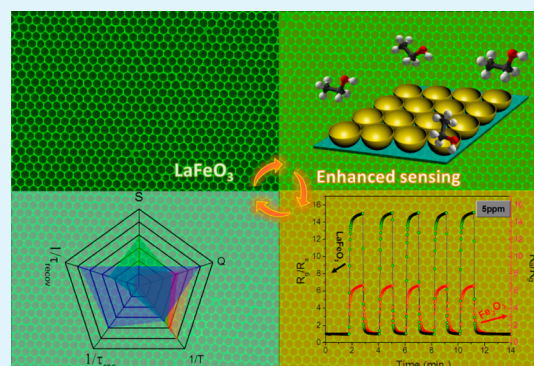
1. INTRODUCTION

The development of high-performance solid-state gas sensors is a topic of increasing interest, because of their extensive applications in a variety of fields, such as food safety, medicine diagnosis, military, and citizen security.[1−3] For remarkable sensitivity and fast response, semiconducting metal oxides (SMOs) have been indicated as the most promising materials, which can easily award sensors with irreplaceable merits of low cost, simple fabrication, direct electrical readout, and good compatibility with Si processes.[4,5] With respect to SMO sensor, the gas response is manifested by the change in electric conductance resulting from the interaction between the adsorbed target gas molecules and active sites on the sensing film surface.[6,7] Hence, it is well-understood that both chemical component and microstructural feature play significant roles in the final gas-sensing characteristics.[8,9]

In recent years, nanostructured metal oxides are highly intriguing in gas sensing properties.[10] They can easily possess the increased surface-to-volume ratios, larger portion of near-surface regions with high chemiresistive variation, more surface active sites, and strong adsorption to the target gas molecules.[11,12] Far-ranging gases and vapors can be detected and monitored with enhanced performances by SMO sensors based on a rich variety of nanostructures, such as 0D (zero-dimensional) nanoparticles,[13] 1D nanowires, and 2-D nano-sheets.[14−16] For practical applications, these nano-objects (nanoparticles, nanowires, nanosheets, etc.) often need to be prepared in the form of thin films, preferably on insulating substrate with conductive electrodes for electrical addressing and monitoring.[17] However, these porous thin films are usually fabricated on sensor substrates via drop-casting or brush-coating.[18] This often leads to inhomogeneous film thickness, irreproducible fabrication, instable microstructure, and thus weak repeatability of gas sensing performances. It remains a challenge in facile fabrication of nanostructured sensing films with controllable microstructure and uniform thickness. More recently, it has been depicted that micro/nanostructured ordered porous thin films are good candidates to solve above problems.[19,20] Employing the self-assembled colloidal crystal templates,[21,22] ordered porous thin films with homogeneous layouts can be simply fabricated on some desired substrates via solution-dipping,[23] sputtering,[24] hydrothermal methods, and so
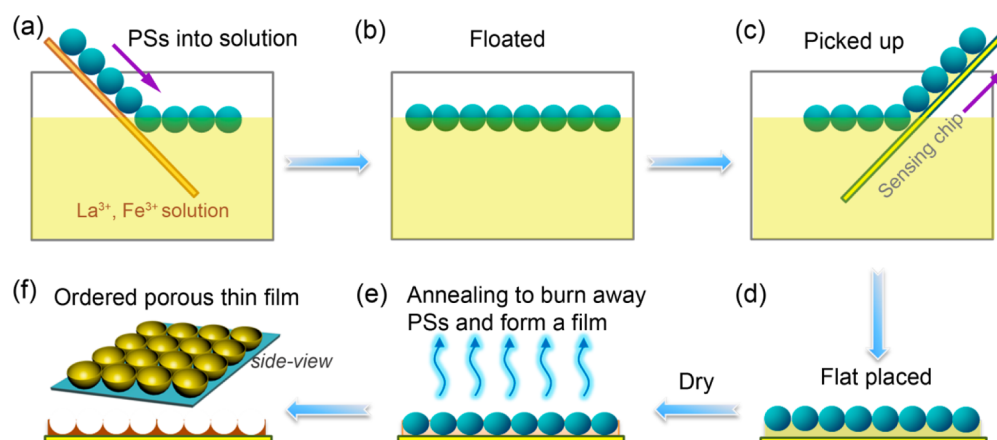
Figure 1. Schematic illustration of the fabrication strategy for honeycomb-like $LaFeO_3$ ordered porous thin films. (a) Flat glass slide covered with a colloidal monolayer consisted of PS spheres (PSs) is slowly dipped into a mixed precursor solution containing La^{3+} and Fe^{3+}. (b) Colloidal monolayer floating on the surface of the mixed solution. (c) Floating monolayer is picked up using a sensing substrate. (d) Substrate covered with the monolayer is placed and dried. (e) Dried sample is treated with high-temperature annealing to remove PSs spheres and form a film. (f) Honeycomb-like $LaFeO_3$ ordered porous thin films are synthesized on the substrate after heating treatment.

forth.[25] Importantly, these template-directed ordered micro/nanostructured films can also exhibit superior gas sensing properties than those of nontemplated dense and thick ones, because of their excellent gas accessibility and high surface area.[26]

As mentioned above, besides the microstructural features, gas sensing properties can also be tuned significantly by the chemical components.[27−29] Present studies on nanostructured SMO sensors have mostly concentrated on systems consisting of single metal oxide (usually SnO_2, ZnO, In_2O_3, etc.).[30−33] The disadvantage of such sensors is the relatively low selectivity to gases that have similar chemical characteristics. In this context, the use of composite materials and polynary compounds can be a viable alternative to improve conductometric sensors.[34−37] Recently, perovskite oxides, ABO_3, have been considered as excellent candidates for a series of technical field applications ranging from catalysts and gas separation to solar cells as well as gas sensing,[38−40] because of their both multiple functionalities (catalytic, magnetic) and chemical, thermal, and mechanical stability.[41] Many compositional combinations between A-oxide and B-oxide with different acid/base properties, catalytic activities, and electrical properties provide a unique strategy to design high performance gas sensors. Moreover, defects in ABO_3 generated from cation deficiency in either A or B sites or oxygen deficiency can be well-manipulated by partial substitution for $A_xA'_{1-x}B_yB'_{1-y}O_3$ compounds with tuned structural, catalytic, and electrical properties.[28] Indeed, perovskite oxides (typically, $LaFeO_3$) with rich oxygen deficiencies can easily realize the favorable sensing characteristics.[42−45] For instance, Simon et al. have prepared a series of nanoparticulate $LnMO_3$ (Ln = La, Pr, Nd, Sm, etc.; M = Fe, Cr) oxides via polyol-mediated synthesis, indicating a controllable sensing behaviors via chemical tuning;[42] in our previous work,[43] we also demonstrated that $LaNiO_3$ nanofiber mats with p-type characteristics exhibited a remarkably high selectivity for EtOH against interfering CO, H_2, NH_3, and NO_2 gases. Nevertheless, sensing performances based on perovskite oxides, such as $LaFeO_3$, with template-directed homogeneous microstructures, possibly favorable for high performance with good stability, have been barely investigated.

In this work, a sacrificial colloidal template approach is exploited to synthesize crystalline ternary $LaFeO_3$ perovskite porous thin films, by transferring a $La^{3+}−Fe^{3+}$ hybrid solution-dipped monolayer template array onto a substrate and sequent heat treatment. Honeycomb-like porous $LaFeO_3$ film can be successfully in situ synthesized in a homogeneous layout with a single phase of perovskite. Such a $LaFeO_3$ porous film, a p-type material, exhibits enhanced sensing performances than those of a binary n-type Fe_2O_3 porous film as well as dense $LaFeO_3$ film. In addition, a five-axe spiderweb diagram is introduced to make a feasible evaluation of the optimal practical work condition. The synthetic method for periodic porous $LaFeO_3$ monolayer not only provides a general chemical route to fabricate various multicompositional periodic porous thin films, but also can be applied to many fields of applications, such as solar cells, ion conductors, gas separation, piezoelectricity, and self-powered sensing device system.

2. EXPERIMENTAL SECTION

Preparation of Monolayer Porous Film. Glass slides (7.5×2.5 cm^2), with 2 mm in thickness, were cleaned according to the procedures reported previously.[21] Suspension of monodispersed polystyrene sphere (PS) with 500 nm in diameter (2.5 wt % in water) was purchased from Alfa Aesar Corporation. The PS colloidal monolayer template was prepared on the well-cleaned glass slide by air/water interfacial assembly.[21] A $La(NO_3)_3$ and $Fe(NO_3)_3$ mixed solution (molar ratio of La and Fe, 1:1) with total cation concentration 0.1 M was used as the precursor solution. On the basis of the solution-dipping route shown in Figure 1, the PS monolayer floating on the solution surface was picked up with the desired substrates, such as silicon wafer, glass, and alumina sensor substrate with two Au electrodes (widths: 0.25 mm, separation: 0.15 mm) and a microheater on its bottom surface, and flat-placed for 10 min and then dried at 110 °C for 0.5 h in an oven. For the sensing substrates, to avoid the deposition of the precursors on the underneath heater, we used the wet cotton swab to wipe the precursors film carefully. Finally, the dried substrate covered with the PS monolayer was transferred in a furnace at 600 °C for 3 h to burn the PS spheres away and meantime form honeycomb-like porous $LaFeO_3$ thin films. In addition, 0.1 M $Fe(NO_3)_3$ is also adopted to synthesize n-type Fe_2O_3 order porous thin film and prepare another sensor for comparison.

Characterization. The morphologies and microstructures of the samples were examined on a field-emission scanning electron microscope (FESEM, S-4700, Hitachi Co. Ltd., Japan) and a

transmission electron microscope (TEM, JEM-ARM-200F, JEOL, USA). Phase analysis of the films was carried out on a grazing incidence geometry X-ray diffraction (XRD, D/MAX-2500 V/PC, Rigaku, Japan) using Cu Kα (0.15419 nm) radiation with the incidence angle 0.3°. X-ray photoelectron spectrum (XPS) analysis was conducted using an Al Kα X-ray source on a Thermo-VG MULTILAB 2000 spectrometer. The n-type silicon ⟨100⟩ substrate was used to coat porous films for FESEM, XRD, and XPS analyses.

Gas-Sensing Measurements. Sensor devices were built by in situ fabrication of order porous thin films, such as LaFeO$_3$ and Fe$_2$O$_3$, on the above-mentioned alumina substrates. The gas sensing experiments were carried out in a dynamical gas sensing system with a 5−1/2 digit picoammeter/voltage source (Keithley mod. 6487). The sensor temperatures could be controlled using the microheater underneath the substrate and measured using an IR temperature sensor (Metis MP25, Sensortherm GmBH, Germany). The gas concentrations were independently controlled by mixing between gases (in air balance) and dry air, and a constant flow rate of 500 sccm was employed. The sensing response was obtained by measuring the change of the electrical resistance of the sensing devices by Keithley 6487 picoammeter.

3. RESULTS AND DISCUSSION

Fabrication Strategy. Based on the colloidal crystal template, we present a facile template-transferring and solution-dipping strategy for ternary LaFeO$_3$ perovskite periodic micro/nanoporous thin films, as shown in Figure 1. It starts from a glass slide covered with the self-organized polystyrene (PS) colloidal monolayer (see Figure S1a in the Supporting Information). This slide is slowly dipped into a mixed precursor solution with the concentration ratio of Fe^{3+} and La^{3+} 1:1 (Figure 1a). Then, such a monolayer can be integrally lifted off from its glass substrate, because of its hydrophobicity and solution surface tension, and floated on surface of the solution (Figure 1b). Subsequently, the floating monolayer is picked up using a desired substrate (Figure 1c). The picked monolayer should also contain the solution in the interstitials due to the capillarity. The substrate covered with the monolayer is then placed and subsequently dried at a certain temperature (Figure 1d). Then, the as-dried sample is placed into a furnace to burn off the PS spheres and meanwhile form a homogeneous metal-oxide thin film (Figure 1e). After annealing treatment, the micro/nanostructured ordered porous lanthanum ferrite thin films can thus be in situ synthesized on the substrates we need (Figure 1f). Figure S1b in the Supporting Information presents a photo of as-synthesized LaFeO$_3$ porous thin film on the Si substrate based on the in situ sacrificial template strategy. It displays iridescent color originating from diffraction effect of the thin film, indicating a formation of periodic LaFeO$_3$ pore arrays. On the basis of this strategy with the same procedures, the periodic porous Fe$_2$O$_3$ thin films can also be in situ synthesized using Fe^{3+} precursor solution for reference.

Phase, Morphology, and Chemical State. Figure 2 shows the XRD patterns of the as-synthesized LaFeO$_3$ and Fe$_2$O$_3$ thin films by the sacrificial colloidal template approach (Figure 1). In the case of Fe$_2$O$_3$ porous film, the main peaks observed at crystalline planes, as well as other small peaks, coincide with the standard α-Fe$_2$O$_3$ card file (JCPDS No. 33−0664). For the LaFeO$_3$ sample, all the peaks are well-matched with the standard JCPDS card of LaFeO$_3$ (No. 75−0541), indicating a single octahedral perovskite phase.[46] The mean crystallite sizes of LaFeO$_3$ and Fe$_2$O$_3$ are calculated as about 20.4 and 23.5 nm by the Scherrer equation, respectively. There are no miscellaneous peaks in the spectra of both samples. This
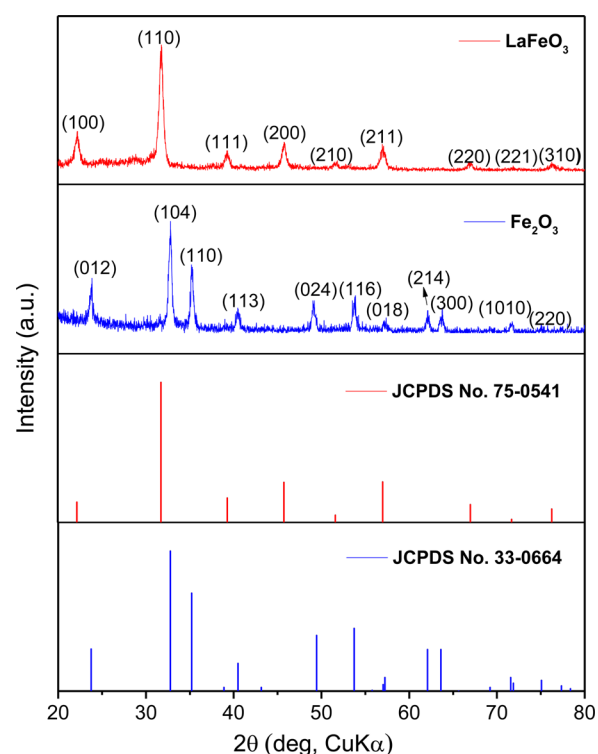

Figure 2. XRD spectra of the as-synthesized LaFeO$_3$ and Fe$_2$O$_3$ porous thin films, respectively.

confirms that such a solution-dipping sacrificial template route provides a facile synthetic route to prepare multicomponent porous oxide films successfully.

Further, we have investigated the morphologies and microstructures of these template-directed LaFeO$_3$ and Fe$_2$O$_3$ porous thin films (Figure 3). A typical SEM image of a self-organized PS colloidal crystal monolayer on the Si substrate is presented in Figure 3a. The monolayer is composed of PS spheres (500 nm in diameter) with hexagonal close-packed arrangement. The high-quality colloidal sphere monolayer can acknowledge a superior film of good homogeneity. Figure 3b shows the SEM image of the template-directed LaFeO$_3$ porous thin film. The porous thin film is visually crack-free, and characterizes as a homogeneous honeycomb-shaped array. A corresponding two-dimensional Fourier transform of the 40 × 26 μm^2 area of this LaFeO$_3$ ordered porous film is performed with a fast Fourier transformation (FFT) filter in image processing software, as depicted in the inset of Figure 3b. These distinct uniform hexagonal spots clearly state that the porous LaFeO$_3$ monolayer exhibits a long-range order in nature with hexagonally ordered pore arrangements, revealing a perfect template-replica process. It is also confirmed further by the corresponding high-magnification SEM image (Figure 3c). The cross-sectional view of the LaFeO$_3$ monolayer film readily demonstrates that the thickness of the pore walls and the height are about 28 and 192 nm (see the bottom inset of Figure 3c), respectively. The interior and geometrical structures of as-obtained honeycomb-like LaFeO$_3$ pore arrays are further elucidated by transmission electron microscopy (TEM) (Figures 3d, e). In accordance with the SEM features, hexagonally ordered pores are clearly revealed in the TEM image of LaFeO$_3$ porous thin film (Figure 3d), and numerous mesopores can be obviously observed within the pore skeleton (marked with arrows in Figure 3e). The formation of these
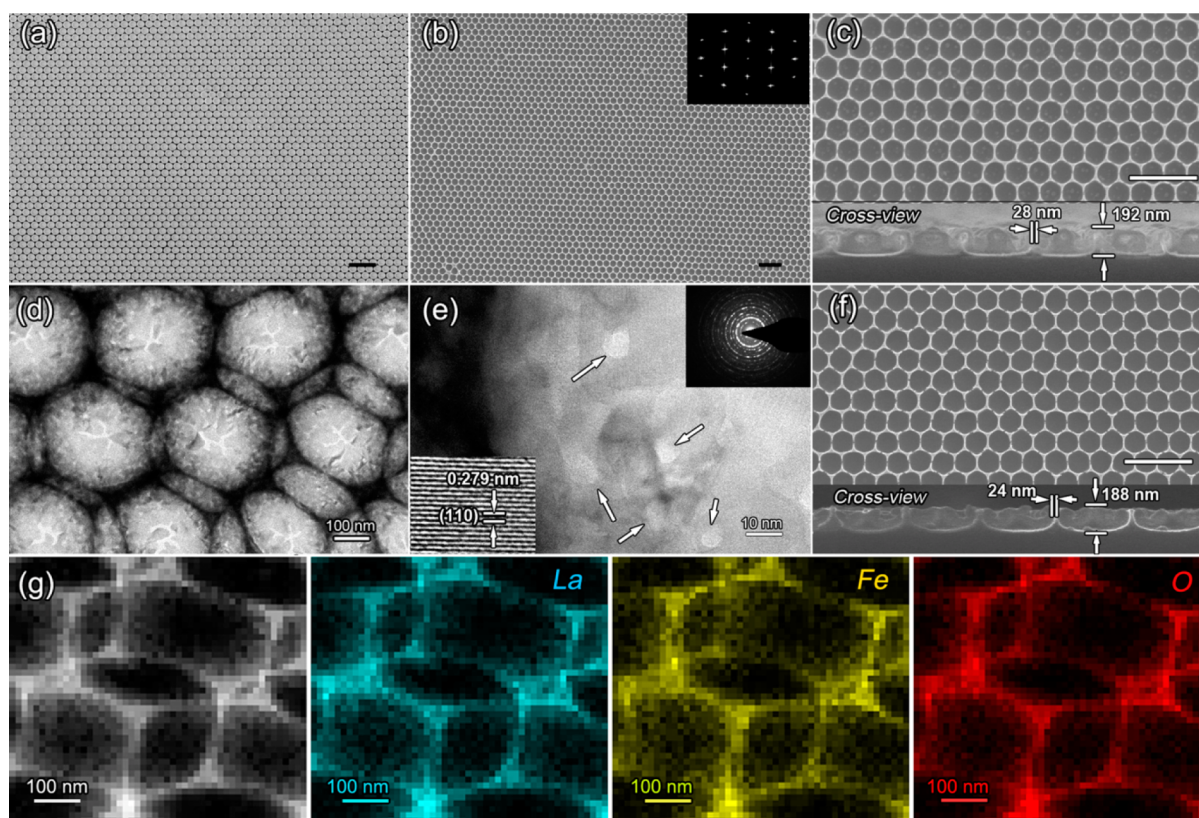
16219

dx.doi.org/10.1021/am504386q | ACS Appl. Mater. Interfaces 2014, 6, 16217−16226

Figure 3. Morphological and microstructural characterizations of the honeycomb-like $LaFeO_3$ and Fe_2O_3 ordered porous thin films. (a) Typical SEM image of a PS microsphere (500 nm in diameter) monolayer; (b) typical SEM image of the $LaFeO_3$ ordered porous film and the corresponding Fourier transform image (inset); (c) high-magnification image of b and the corresponding cross view (inset); (d, e) TEM observations with different magnifications and the insets in (e): HRTEM image (bottom) and SAED pattern (upper); (f) high-magnified SEM image of Fe_2O_3 ordered porous thin films and the corresponding cross view (inset); (g) elemental mapping showing the homogeneous dispersion of La, Fe, and O element in $LaFeO_3$ pores. The scale bars if no specification are 2 μm.

mesopores may be attributed to the degassing by the decomposition of polystyrene template during heat treatment.

A high-resolution TEM (HRTEM) image (the bottom inset of Figure 3e) clearly shows the $LaFeO_3$ grain with the fringe-spacing of 0.279 nm corresponding to (110) plane. Meantime, the corresponding selected-area electron diffraction (SAED) pattern has demonstrated a polycrystalline $LaFeO_3$ structure (the upper inset of Figure 3e), which shows a good agreement with the XRD result. In addition, an n-type honeycomb-like Fe_2O_3 porous thin film is also synthesized for comparison using $Fe(NO_3)_3$ precursor by the same method. Its morphology (Figure 3f) is similar to the former $LaFeO_3$ sample (Figure 3c), and the cross-section image illustrates the wall thickness and the Fe_2O_3 film height are about 24 and 188 nm, respectively (see the bottom inset of Figure 3f). For a polynary material system, sometimes a phase separation and/or elements segregation will occur in in the film body, which always have negative impacts on the related properties.[47] For the single perovskite phase $LaFeO_3$ film (Figure 2), the elemental mapping measurement further confirms the coexistence and homogeneous dispersion of La, Fe and O elements within the pores (Figure 3g).

The chemical composition and the valence state of the elements in the $LaFeO_3$ porous thin film have been examined by X-ray photoelectron spectroscopy (XPS). Figure 4a shows the typical XPS survey spectra of La(3d), Fe(2p), O(1s), and C(1s) for the $LaFeO_3$ film. The binding energies obtained in the XPS analysis were corrected for specimen charging by

referencing the C 1s line to 284.5 eV. The La 3d doublet located at 834.0 and 850.8 eV (Figure 4b), which are ascribed to La—O bonds of $3d_{5/2}$ and $3d_{3/2}$. Each doublet is further split into two components, due to the charge transfer from the ligand 2p level to the La 4f level.[48] The spin−orbit splitting gap of ~16.8 eV between $3d_{3/2}$ and $3d_{5/2}$ peaks is also indicative of the La^{3+} state.[48] In the Fe 2p spectrum (Figure 4c), two distinct peaks at binding energies of ~710.2 eV for Fe $2p_{3/2}$ and ~723.7 eV for Fe $2p_{1/2}$ with a shakeup satellite at ~718.9 eV are observed, which corresponds to the characteristic of Fe^{3+} ions in their oxide form.[49] Results from deconvolution of the O 1s binding energy spectrum suggest two peaks at 528.6 and 531.1 eV that are attributed to lattice oxygen $O_{lattice}$ (O^{2-}) and surface adsorbed oxygen O_{ads} (e.g., O^-).[50] In addition, XPS spectra of Fe_2O_3 porous thin films are shown in Figure S2 in the Supporting Information, which also indicates the Fe^{3+} state of α-Fe_2O_3.[51] Obviously, the relative intensity of $[O_{ads}]/[O_{lattice}]$ of the $LaFeO_3$ film (Figure 4d) is higher than the Fe_2O_3 sample (seeFigure S2b in the Supporting Information), which corresponds larger populations of surface oxygen species of $LaFeO_3$ porous film. All above results confirm that the solution-dipping template approach can be a facile and effective way to form $LaFeO_3$ porous thin films by using a Fe^{3+}−La^{3+} mixed solution precursor. Such periodic micro/nanopores array and the rich interior mesopores as well as enhanced surface oxygen species could possibly benefit the gas sensing response, which is favorable for the gas-oxide interactions.[52−55]
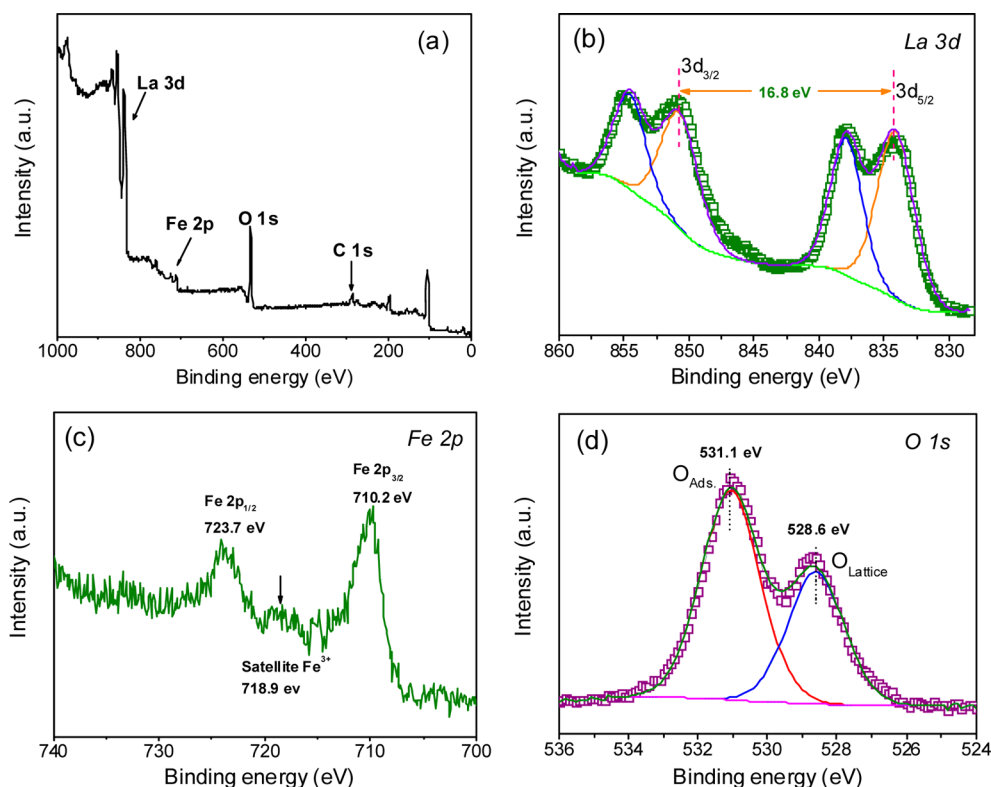
Figure 4. XPS spectra of LaFeO$_3$ porous film. (a) Survey spectrum; (b) Fe 2p binding energy spectrum; (c) La 3d binding energy spectrum; (d) O 1s core level spectrum.

Enhanced Gas-Sensing Characteristics. According to the strategy in Figure 1, we in situ fabricated the honeycomb-like LaFeO$_3$ and Fe$_2$O$_3$ porous thin films on alumina substrate with two Au electrodes and a microheater to construct gas sensing devices. Herein, the R_g/R_a and R_a/R_g values (R_g, resistance in gas; R_a, resistance in air) are defined as the real-time gas responses for p-type and n-type SMO sensors, respectively; and the steady gas responses (S) are calculated using the maximum (in p-type) or minimum (in n-type) value of resistance in gas (R_G). And the response time (τ_{res}) and recovery time (τ_{recov}) are fixed as the time spans to reach a 90% variation in resistance upon exposure to gas and air, respectively.[23] Figure 5 presents the dynamic sensing transients of ternary LaFeO$_3$ and binary Fe$_2$O$_3$ sensors toward 5 ppm different gases at 450 °C, respectively. The corresponding R_a of the LaFeO$_3$ sensor is observed as 1.5 MΩ that is almost 150 times lower than R_a of the Fe$_2$O$_3$ sensor (220 MΩ), showing a preferable electric measurement with lower Johnson noise (as a square root of the resistance value).[56]

When exposing to reducing gas (e.g., EtOH), the LaFeO$_3$ sample with increasing resistance behaves as a typical p-type SMO sensor. Remarkably, this p-type LaFeO$_3$ sensor displays a superior sensing response to ethanol gas than other gases, such as acetone, toluene, p-xylene (PX), formaldehyde, ammonia, CO, and H$_2$. The response to 5 ppm EtOH is ~15, much higher than acetone response (S = 4.5), and the response (τ_{res}) and recovery time (τ_{recov}) are ~6 and 5 s, respectively. These indicate that the LaFeO$_3$ sensor not only exhibits high response and selectivity to EtOH, but also possesses fast responding and recovering speed. For comparison, the gas sensing properties of the porous Fe$_2$O$_3$ sample were also investigated at the same conditions. It demonstrates the opposite tendency of resistance variation against the LaFeO$_3$ one, manifesting an n-type metal
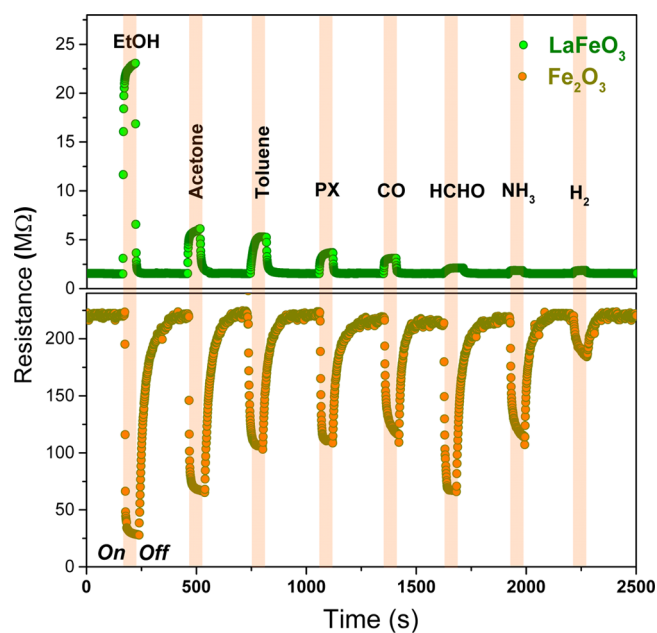

Figure 5. Dynamic sensing transients of the honeycomb-like LaFeO$_3$ (upper) and Fe$_2$O$_3$ (bottom) thin film sensors toward 5 ppm different gases at 450 °C, respectively.

oxide characteristic. The response of Fe$_2$O$_3$ sensor to 5 ppm EtOH is ~6.5, and τ_{res} and τ_{recov} are ~6 and 71 s, respectively. The bar plot of Figure S3 in the Supporting Information compares the τ_{res} and τ_{recov} values of LaFeO$_3$ sensor and Fe$_2$O$_3$ sensor to different gases, respectively. The τ_{res} values of Fe$_2$O$_3$ sensor are more than 10 s to most gases other than EtOH (see Figure S3a in the Supporting Information). In especial, its

16221

dx.doi.org/10.1021/am504386q | ACS Appl. Mater. Interfaces 2014, 6, 16217−16226
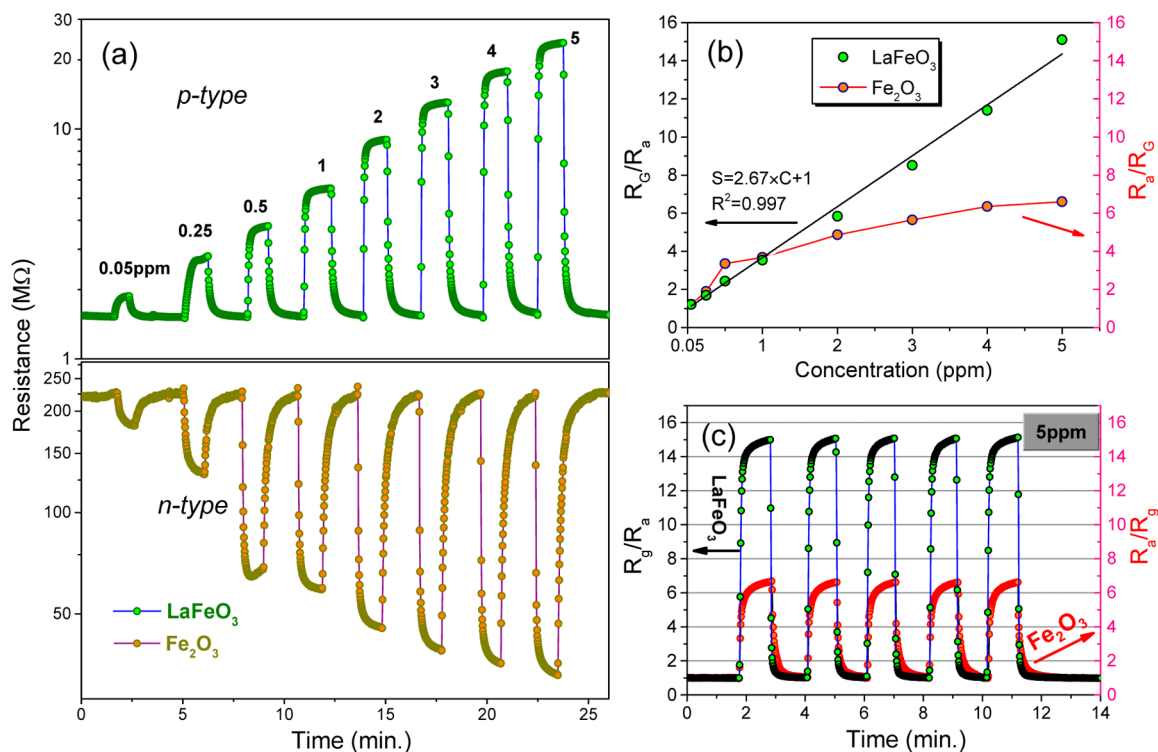
Figure 6. EtOH-sensing properties of the honeycomb-like LaFeO₃ and Fe₂O₃ porous thin film sensors at 450 °C. (a) Dynamic sensing transients to 0.05−5 ppm EtOH; (b) response of each sensor as a function of EtOH gas concentration; (c) sensing responses for 5 gas-on/off circles to 5 ppm EtOH.
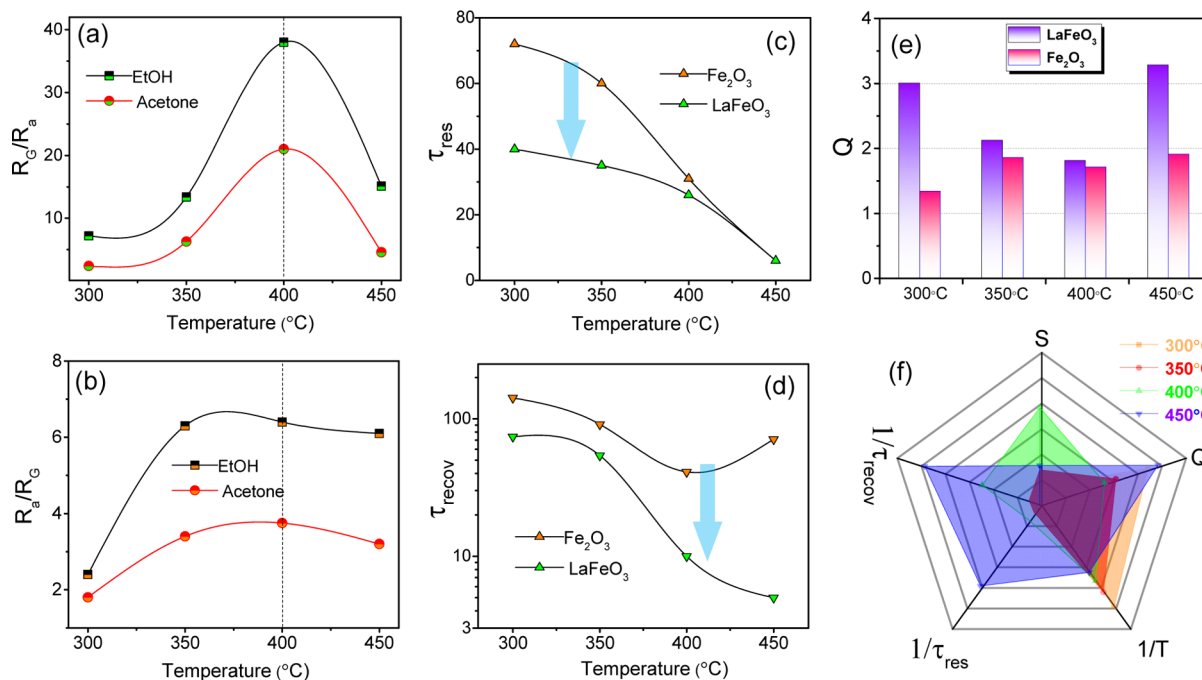

Figure 7. Comprehensive investigations of both honeycomb-like LaFeO₃ and Fe₂O₃ thin film sensors performances at different working temperatures. (a, b) show the dependence of the sensitivities (5 ppm) on the working temperatures of LaFeO₃ and Fe₂O₃ sensors, respectively. (c, d) list the response and recovery times to 5 ppm EtOH in 300−450 °C, respectively. (e) Bar graph summarizing the EtOH/acetone selectivity (Q) in 300−450 °C. (f) Five-axe spiderweb diagram for evaluating the optimal work condition of LaFeO₃ sensor. The different colors represent different operating temperature: orange for 300 °C, red for 350 °C, green for 400 °C, and violet for 450 °C.

recoveries times are around tens of seconds (see Figure S3b in the Supporting Information) that are much longer than the LaFeO₃ one, and also the response differences between HCHO, acetone and EtOH responses are insignificant for the

Fe₂O₃ sensor (lower graph in Figure 5). In addition, to investigate the merit of ordered porous morphology, we have also prepared a nontemplated dense and thick LaFeO₃ film by solution spin-coating on substrate without sacrificial templates

and subsequent annealing (see Figure S4 in the Supporting Information), and then measured its gas sensing properties (see Figure S5a in the Supporting Information). The bar plot in Figure S5b in the Supporting Information also demonstrates the inferior gas sensing responses of the nontemplated dense $LaFeO_3$ thick film comparing with the templated porous $LaFeO_3$ thin film sensors. Hence, it can be concluded that the ternary $LaFeO_3$ porous film conducts the enhanced sensing performances than those of the binary Fe_2O_3 sample and nontemplated dense and thick $LaFeO_3$ film, such as a faster recovery, higher EtOH response, and selectivity.

Figure 6a shows the dynamic sensing transients to 0.05−5 ppm EtOH for $LaFeO_3$ and Fe_2O_3 sensing devices at 450 °C, respectively. Both of the sensors express the good capacity of fast distinguishing trace ethanol gas ($S = 1.22$) as low as 50 ppb. Figure 6b shows EtOH response of each sensor as a function of gas concentration. A linear response vs concentration trend can be better observed for the $LaFeO_3$ sensor, showing a better potential in the quantitative gas analysis. Such dependence can be well-described by the empirical equation of SMO gas sensors[23]

$$A = A_g C^\beta + 1 \qquad (1)$$

where A_g represents a constant, and C is the concentration of the target gas. The power exponent (β) is the parameter (usually from 0.5 to 1) depending on the charge of the surface species and the stoichiometry of the elementary reactions on the surface. Hence, a linear fitting dependence in the 0.05−5 ppm range of the porous $LaFeO_3$ sensor is addressed as below

$$S = 2.671C + 1 \qquad (2)$$

.Further, we have investigated the stability and reproducibility for such gas-sensing devices. Figure 6c plots their sensing responses for 5 gas-on/off circles to 5 ppm EtOH at 450 °C. Both sensors exhibit good reproducibility, because of the merits of the honeycomb-like ordered porous thin films induced from in situ template method.[20]

Optimal Working Condition. In general, metal-oxide semiconductors need heating to proper temperatures so as to obtain optimum gas response.[57] Panels a and b in Figure 7 represent the dependence of gas responses on the working temperatures of honeycomb-like $LaFeO_3$ and Fe_2O_3 thin film sensors, respectively. It can be easily observed that the optimal temperature for highest responses of each sensor to acetone and EtOH gas is ∼400 °C. The response of the $LaFeO_3$ sensor to 5 ppm EtOH reaches as high as 38 (Figure 7a), whereas the response of the Fe_2O_3 sensor is ∼6.4 at 400 °C (Figure 7b). However, such a $LaFeO_3$ sensor also displays a degraded selectivity to EtOH at 400 °C, because of the much increased acetone and HCHO responses (see Figure S6 in the Supporting Information). Further, we have investigated the τ_{res} and τ_{recov} values upon exposures to 5 ppm EtOH and air, respectively, at the working temperature range from 300 to 450 °C (Figure 7c, d). When decreasing the temperature to 400 °C, the responding speed of $LaFeO_3$ sensor upon exposure to EtOH becomes sluggish ($\tau_{res} = 26$ s) despite preserving a fast recovery rate ($\tau_{recov} = 10$ s). From these curves, it is found that the $LaFeO_3$ sensor always exhibits a faster EtOH responding/ recovering kinetic than the Fe_2O_3 sample throughout the 300− 450 °C range. And also the increasing temperature shortens the response and recovery times of $LaFeO_3$ sensor, which is probably due to the thermal promotion of surface reaction for gas sensing. Herein, it is indicated the best temperature with

high response is 400 °C whereas the optimal temperature with fastest sensing kinetic is 450 °C, for the $LaFeO_3$ sensor.

The bar plot of Figure 7e summarizes 5 ppm EtOH-responses of $LaFeO_3$ and Fe_2O_3 sensors at 300−450 °C range. Here the selectivity (Q) is defined as the EtOH response (S_{EtOH}) divided by the acetone response ($S_{Acetone}$), or $Q = S_{EtOH}/S_{Acetone}$. The height of each bar represents the corresponding value of EtOH response from interfering acetone (5 ppm). For the Fe_2O_3 sensor, the Q value is below 2 all along the temperature range, indicating a weak EtOH selective detection capacity. However, the $LaFeO_3$ sensor displays a favorable selectivity with $Q \geq 3$ at 450 °C ($Q = 3.28$) or 300 °C ($Q = 3.01$), if consuming $S_{Acetone}$ as a noise of the S_{EtOH} signal and thus Q as signal-to-noise ratio (S/N). In spite of Q appropriate for EtOH selectivity at low 300 °C, it remains a challenge for the practical applications because of the long response and recovery time ($\tau_{res} = 40$ s and $\tau_{recov} = 74$ s, see Figure 7c, d). At 450 °C, besides the rapid sensing kinetics, the $LaFeO_3$ sensor also endows a highest selectivity capacity.

For SMO sensors, the optimum temperature for high response is always not seemly for gaining the fastest response/recovery rates and highest selectivity simultaneously.[14,32] This incompatibility challenges one to determine the optimal working temperature or condition toward balanced performances. To address this issue, a five-axe spiderweb diagram is introduced to make a feasible evaluation of the optimal practical work condition, comprehensively regarding the response/recovery rate ($1/\tau_{res}$ and $1/\tau_{recov}$), response (S), selectivity (Q) and operating temperature ($1/T$), as depicted in Figure 7f. The larger values on each axe in the spiderweb, the more excellent a sensor will be. In the case of $LaFeO_3$ sensor, it is visible that the blue area (450 °C) in the spiderweb diagram is larger than other color area or other working temperatures, clearly indicating that the 450 °C is the optimal working condition with more balanced sensing performances, such as preferable response, fast response/recovery, and high selectivity. This spiderweb diagram can provide an alternative way to make effective evaluations of the sensing properties and determine the optimal working condition toward balanced high performances.

Enhanced Sensing Mechanism. As mentioned above, the ternary $LaFeO_3$ porous thin film conducts the enhanced EtOH sensing response than that of the binary Fe_2O_3 sample. With respect to SMO sensors, their sensing performances mainly depend on the type of materials and their surface physical/ chemical properties, such as surface basic/acidic properties and surface groups (e.g., O_2^-, O^-). In general, the mechanism of reductive gases detection undergoes an adsorption−oxidation process. When sensor exposed to reducing gases (e.g., EtOH gas), the ethanol molecules are oxidized by oxygen species into CO_2 and H_2O, and simultaneously the electrons are fed back into sensing body (see reaction 3), leading to a depletion of holes and thus an increased resistance for p-type sensor (reaction 4).[58]

$$C_2H_5OH + 6O^- = 2CO_2 + 3H_2O + 6e^- \qquad (3)$$

,

$$h^+ + e^- = null \qquad (4)$$
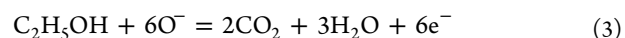
.Interactions of ethanol molecules with oxide surfaces are quite complicate, and the sensing response concerns about the nature of the surface active centers. From previous protocols,[59,60] the ethanol molecules can convert to CO_2 and H_2O through two

types of reactions: (i) dehydration into C_2H_4 in the presence of acid surface groups as shown in reaction 5; and (ii) dehydrogenation into CH_3CHO with the assistant of basic surface groups as illustrated in reaction 6. And then the intermediates (C_2H_4, CH_3CHO, and H_2) will react with chemisorbed oxygen ions and transform into CO_2 and H_2O.

$$C_2H_5OH \xrightarrow{\text{acidic}} C_2H_4 + H_2O \tag{5}$$

$$C_2H_5OH \xrightarrow{\text{basic}} CH_3CHO + H_2 \tag{6}$$
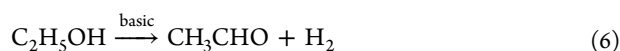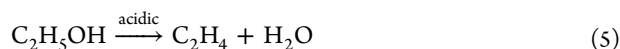
According to reactions 5 and 6, metal oxides with acidic (e.g., SnO_2 and WO_3), amphoteric (e.g., Fe_2O_3 and ZrO_2), and basic (e.g., MgO and La_2O_3) surfaces involve different interaction procedures and different sensing behaviors.[61] The surface of amphoteric Fe_2O_3 porous film contains both of Lewis acidic and basic centers, and thus EtOH molecules mainly decompose both to C_2H_4 and CH_3CHO intermediates. On the other side, the addition of the typical basic La will reduce the amount of the acidic sites and make the ternary $LaFeO_3$ film more basic. From the thermodynamic point of view, reaction 6 is more favorable than reaction 5 under the same conditions.[59] It will result in a preferred dehydrogenation process that makes more ethanol molecules convert to CH_3CHO and H_2. The mixture between CH_3CHO and H_2 is much active than the mixture of C_2H_4 and H_2O and hence will be better for conversion into CO_2 and H_2O.[62] From the observation of phase and morphology, the grain size, wall thickness and film thickness of the two films are similar, so these factors will show very little influences on the sensing response differences. Hence, owing to the more surface basicity and oxygen groups, the $LaFeO_3$ porous thin film shows an enhanced EtOH sensing response than the Fe_2O_3 porous film. In the literature, the values of lowest unoccupied molecule orbit (LUMO) energy of different volatile organic compounds can used as index to show the easiness of gas sensing reaction.[63] Very low LUMO energy value of EtOH may explain the selective detection of EtOH in the present study. In addition, the enrichment of adsorbed oxygen groups probably plays a noteworthy role in the recovery kinetics p-type oxide which involves the in-diffusion of oxygen gas to the sensor surface and subsequent surface reactions such as the adsorption, dissociation, and ionization of the oxygen.[58] The surface reactions, the rate-determining step when a gas rapidly diffuses, that form the oxygen anions on the surface of the sensor material can be accelerated with the abundant adsorbed oxygens, as indicated like our case of p-type $LaFeO_3$ vs n-type Fe_2O_3.

4. CONCLUSION

In summary, a sacrificial colloidal template approach is exploited to synthesize crystalline ternary honeycomb-like $LaFeO_3$ perovskite porous thin films, by transferring a La^{3+}– Fe^{3+} hybrid solution-dipped template onto a substrate and sequent heat treatment. It is indicated that the honeycomb-like $LaFeO_3$ film can be successfully in situ synthesized in a homogeneous layout and a single phase of perovskite. Further, we have investigated the sensing properties of the ternary $LaFeO_3$ ordered porous thin film and made a comparison with a Fe_2O_3 film. Such a $LaFeO_3$ porous film, a p-type material, exhibits a high sensitivity, fast response (~4 s), trace detection capacity (50 ppb), and favorable selectivity to ethanol from the similar gas acetone, showing enhanced sensing performances than those of a binary n-type Fe_2O_3 film and also nontemplated

dense $LaFeO_3$ film. In addition, a five-axe spiderweb diagram is introduced to make a feasible evaluation for the optimal practical work condition, comprehensively regarding the response/recovery rate, sensitivity, selectivity, and operating temperature. A linear response vs concentration trend can be better observed at the $LaFeO_3$ sensor, showing a better potential in the quantitative gas analysis. The enhanced ethanol sensing mechanism of such honeycomb-like $LaFeO_3$ porous film vs Fe_2O_3 is addressed, which accounts for the more surface basicity and increased oxygen groups. This novel and facile chemical route can be also applied to the fabrication of various multicompositional periodic porous thin films and many of distinctive fields of applications, such as solar cells, ion conductors, gas separation, piezoelectricity, and self-powered sensing device system.

■ ASSOCIATED CONTENT

ⓢ Supporting Information
Photographs of PS templated $LaFeO_3$ film; XPS spectra of Fe_2O_3 film; responding and recovering rate; SEM images of nontemplate $LaFeO_3$ films; sensing performance of non-template films; sensing responses at 400 °C. This material is available free of charge via the Internet at http://pubs.acs.org.

■ AUTHOR INFORMATION

Corresponding Author
*E-mail: jongheun@korea.ac.kr. Fax: +82-2-928-3584. Tel: +82-2-3290-3282.

Notes
The authors declare no competing financial interest.

■ ACKNOWLEDGMENTS

■ REFERENCES

(1) Modi, A.; Koratkar, N.; Lass, E.; Wei, B. Q.; Ajayan, P. M. Miniaturized Gas Ionization Sensors Using Carbon Nanotubes. *Nature* 2003, *424*, 171−174.

(2) Kong, J.; Franklin, N. R.; Zhou, C. W.; Chapline, M. G.; Peng, S.; Cho, K. J.; Dai, H. J. Nanotube Molecular Wires as Chemical Sensors. *Science* 2000, *287*, 622−625.

(3) Galli, I.; Bartalini, S.; Borri, S.; Cancio, P.; Mazzotti, D.; De Natale, P.; Giusfredi, G. Molecular Gas Sensing Below Parts Per Trillion: Radiocarbon-Dioxide Optical Detection. *Phys. Rev. Lett.* 2011, *107*, 270802.

(4) Franke, M. E.; Koplin, T. J.; Simon, U. Metal and Metal Oxide Nanoparticles in Chemiresistors: Does the Nanoscale Matter? *Small* 2006, *2*, 36−50.

(5) Potje-Kamloth, K. Semiconductor Junction Gas Sensors. *Chem. Rev.* 2008, *108*, 367−399.

(6) Yamazoe, N.; Shimanoe, K. New Perspectives of Gas Sensor Technology. *Sens. Actuators, B* 2009, *138*, 100−107.

(7) Barsan, N.; Koziej, D.; Weimar, U. Metal oxide-Based Gas Sensor Research: How to? *Sens. Actuators, B* 2007, *121*, 18−35.

(8) Gurlo, A. Nanosensors: Does Crystal Shape Matter? *Small* 2010, *6*, 2077−2079.

(9) Wang, L.; Fei, T.; Lou, Z.; Zhang, T. Three-Dimensional Hierarchical Flowerlike Alpha-Fe2O3 Nanostructures: Synthesis and Ethanol-Sensing Properties. *ACS Appl. Mater. Interfaces* 2011, *3*, 4689−4694.

(10) Lim, M. A.; Kim, D. H.; Park, C. O.; Lee, Y. W.; Han, S. W.; Li, Z. Y.; Williams, R. S.; Park, I. A New Route toward Ultrasensitive, Flexible Chemical Sensors: Metal Nanotubes by Wet-Chemical

16224

dx.doi.org/10.1021/am504386q | *ACS Appl. Mater. Interfaces* 2014, 6, 16217−16226

Synthesis along Sacrificial Nanowire Templates. *ACS Nano* **2012**, *6*, 598−608.

(11) McAlpine, M. C.; Ahmad, H.; Wang, D.; Heath, J. R. Highly Ordered Nanowire Arrays on Plastic Substrates for Ultrasensitive Flexible Chemical Sensors. *Nat. Mater.* **2007**, *6*, 379−384.

(12) Alenezi, M. R.; Henley, S. J.; Emerson, N. G.; Silva, S. R. P. From 1D and 2D ZnO Nanostructures to 3D Hierarchical Structures with Enhanced Gas Sensing Properties. *Nanoscale* **2014**, *6*, 235−247.

(13) Tricoli, A.; Pratsinis, S. E. Dispersed Nanoelectrode Devices. *Nat. Nanotechnol.* **2010**, *5*, 54−60.

(14) Deng, S.; Tjoa, V.; Fan, H. M.; Tan, H. R.; Sayle, D. C.; Olivo, M.; Mhaisalkar, S.; Wei, J.; Sow, C. H. Reduced Graphene Oxide Conjugated Cu_2O Nanowire Mesocrystals for High-Performance NO2 Gas Sensor. *J. Am. Chem. Soc.* **2012**, *134*, 4905−4917.

(15) Choi, S. J.; Lee, I.; Jang, B. H.; Youn, D. Y.; Ryu, W. H.; Park, C. O.; Kim, I. D. Selective Diagnosis of Diabetes Using Pt-Functionalized WO_3 Hemitube Networks as a Sensing Layer of Acetone in Exhaled Breath. *Anal. Chem.* **2013**, *85*, 1792−1796.

(16) Hernandez-Ramirez, F.; Daniel Prades, J.; Hackner, A.; Fischer, T.; Mueller, G.; Mathur, S.; Ramon Morante, J. Miniaturized Ionization Gas Sensors from Single Metal Oxide Nanowires. *Nanoscale* **2011**, *3*, 630−634.

(17) Zhang, W.; Yang, S. In Situ Fabrication of Inorganic Nanowire Arrays Grown from and Aligned on Metal Substrates. *Acc. Chem. Res.* **2009**, *42*, 1617−1627.

(18) Li, X.; Cho, J. H.; Kurup, P.; Gu, Z. Novel Sensor Array Based on Doped Tin Oxide Nanowires for Organic Vapor Detection. *Sens. Actuators, B* **2012**, *162*, 251−258.

(19) Jia, L. C.; Cai, W. P.; Wang, H. Q.; Sun, F. Q.; Li, Y. Hetero-apertured Micro/Nanostructured Ordered Porous Array: Layer-by-Layered Construction and Structure-Induced Sensing Parameter Controllability. *ACS Nano* **2009**, *3*, 2697−2705.

(20) Dai, Z.; Jia, L.; Duan, G.; Li, Y.; Zhang, H.; Wang, J.; Hu, J.; Cai, W. Crack-Free Periodic Porous Thin Films Assisted by Plasma Irradiation at Low Temperature and Their Enhanced Gas-Sensing Performance. *Chem.—Eur. J.* **2013**, *19*, 13387−13395.

(21) Dai, Z.; Li, Y.; Duan, G.; Jia, L.; Cai, W. Phase Diagram, Design of Monolayer Binary Colloidal Crystals, and Their Fabrication Based on Ethanol-Assisted Self-Assembly at the Air/Water Interface. *ACS Nano* **2012**, *6*, 6706−6716.

(22) Jia, L. C.; Cai, W. P. Micro/Nanostructured Ordered Porous Films and Their Structurally Induced Control of the Gas Sensing Performances. *Adv. Funct. Mater.* **2010**, *20*, 3765−3773.

(23) Dai, Z.; Xu, L.; Duan, G.; Li, T.; Zhang, H.; Li, Y.; Wang, Y.; Wang, Y.; Cai, W. Fast-Response, Sensitivitive and Low-Powered Chemosensors by Fusing Nanostructured Porous Thin Film and IDEs-Microheater Chip. *Sci. Rep.* **2013**, *3*, 1669.

(24) Chang, Y.-E.; Youn, D.-Y.; Ankonina, G.; Yang, D.-J.; Kim, H.-G.; Rothschild, A.; Kim, I.-D. Fabrication and Gas Sensing Properties of Hollow SnO_2 Hemispheres. *Chem. Commun.* **2009**, 4019−4021.

(25) Hieu, H. N.; Vuong, N. M.; Jung, H.; Jang, D. M.; Kim, D.; Kim, H.; Hong, S. K. Optimization of a Zinc Oxide Urchin-Like Structure for High-Performance Gas Sensing. *J. Mater. Chem.* **2012**, *22*, 1127−1134.

(26) Kim, I. D.; Rothschild, A.; Hyodo, T.; Tuller, H. L. Microsphere Templating as Means of Enhancing Surface Activity and Gas Sensitivity of $CaCu_3Ti_4O_{12}$ Films. *Nano Lett.* **2006**, *6*, 193−198.

(27) Wang, L.; Dou, H.; Lou, Z.; Zhang, T. Encapsuled nanoreactors $Au@SnO_2$: A New Sensing Material for Chemical Sensors. *Nanoscale* **2013**, *5*, 2686−2691.

(28) Natile, M. M.; Ponzoni, A.; Concina, I.; Glisenti, A. Chemical Tuning versus Microstructure Features in Solid-State Gas Sensors: $LaFe_{1-x}Ga_xO_3$, a Case Study. *Chem. Mater.* **2014**, *26*, 1505−1513.

(29) Lee, J. H. Gas Sensors Using Hierarchical and Hollow Oxide Nanostructures: Overview. *Sens. Actuators, B* **2009**, *140*, 319−336.

(30) Spencer, M. J. S. Gas Sensing Applications of 1D-Nanostructured Zinc Oxide: Insights from Density Functional Theory Calculations. *Prog. Mater. Sci.* **2012**, *57*, 437−486.

(31) Shao, S.; Qiu, X.; He, D.; Koehn, R.; Guan, N.; Lu, X.; Bao, N.; Grimes, C. A. Low Temperature Crystallization of Transparent, Highly Ordered Nanoporous Sno(2) Thin Films: Application to Room-Temperature Hydrogen Sensing. *Nanoscale* **2011**, *3*, 4283−4289.

(32) Zhang, Y.; Xu, J.; Xiang, Q.; Li, H.; Pan, Q.; Xu, P. Brush-Like Hierarchical ZnO Nanostructures: Synthesis, Photoluminescence and Gas Sensor Properties. *J. Phys. Chem. C* **2009**, *113*, 3430−3435.

(33) Wang, X.; Liu, W.; Liu, J.; Wang, F.; Kong, J.; Qiu, S.; He, C.; Luan, L. Synthesis of Nestlike ZnO Hierarchically Porous Structures and Analysis of Their Gas Sensing Properties. *ACS Appl. Mater. Interfaces* **2012**, *4*, 817−825.

(34) Wang, L.; Deng, J.; Lou, Z.; Zhang, T. Cross-linked P-Type Co3O4 Octahedral Nanoparticles in 1D N-Type TiO_2 Nanofibers for High-Performance Sensing Devices. *J. Mater. Chem. A* **2014**, *2*, 10022.

(35) Lou, Z.; Li, F.; Deng, J.; Wang, L.; Zhang, T. Branch-like Hierarchical Heterostructure (α-Fe_2O_3/TiO_2): A Novel Sensing Material for Trimethylamine Gas Sensor. *ACS Appl. Mater. Interfaces* **2013**, *5*, 12310−12316.

(36) Kim, H. R.; Haensch, A.; Kim, I. D.; Barsan, N.; Weimar, U.; Lee, J. H. The Role of NiO Doping in Reducing the Impact of Humidity on the Performance of SnO_2-Based Gas Sensors: Synthesis Strategies, and Phenomenological and Spectroscopic Studies. *Adv. Funct. Mater.* **2011**, *21*, 4456−4463.

(37) Bekermann, D.; Gasparotto, A.; Barreca, D.; Maccato, C.; Comini, E.; Sada, C.; Sberveglieri, G.; Devi, A.; Fischer, R. A. Co_3O_4/ZnO Nanocomposites: From Plasma Synthesis to Gas Sensing Applications. *ACS Appl. Mater. Interfaces* **2012**, *4*, 928−934.

(38) Eerenstein, W.; Mathur, N. D.; Scott, J. F. Multiferroic and Magnetoelectric Materials. *Nature* **2006**, *442*, 759−765.

(39) Liu, D.; Kelly, T. L. Perovskite solar cells with a Planar Heterojunction Structure Prepared Using Room-Temperature Solution Processing Techniques. *Nat. Photonics* **2014**, *8*, 133−138.

(40) Zhang, H.; Song, P.; Han, D.; Wang, Q. Synthesis and Formaldehyde Sensing Performance of LaFeO3 Hollow Nanospheres. *Physica E* **2014**, *63*, 21−26.

(41) Rorvik, P. M.; Grande, T.; Einarsrud, M.-A. One-Dimensional Nanostructures of Ferroelectric Perovskites. *Adv. Mater.* **2011**, *23*, 4007−4034.

(42) Siemons, M.; Leifert, A.; Simon, U. Preparation and gas Sensing Characteristics of Nanoparticulate P-Type Semiconducting $LnFeO_3$ and $LnCrO_3$ Materials. *Adv. Funct. Mater.* **2007**, *17*, 2189−2197.

(43) Hwang, D. K.; Kim, S.; Lee, J.-H.; Hwang, I.-S.; Kim, I.-D. Phase Evolution of Perovskite $LaNiO_3$ Nanofibers for Supercapacitor Application and P-Type Gas Sensing Properties of LaOCl−NiO Composite Nanofibers. *J. Mater. Chem.* **2011**, *21*, 1959−1965.

(44) Zhang, Y. M.; Zhang, J.; Chen, J. L.; Zhu, Z. Q.; Liu, Q. J. Improvement of Response to Formaldehyde at Ag−LaFeO3 Based Gas Sensors through Incorporation of Swcnts. *Sens. Actuators, B* **2014**, *195*, 509−514.

(45) Toan, N. N.; Saukko, S.; Lantto, V. Gas Sensing with Semiconducting Perovskite Oxide $LaFeO_3$. *Physica B* **2003**, *327*, 279−282.

(46) Fan, H.; Zhang, T.; Xu, X.; Lv, N. Fabrication of N-type Fe_2O_3 and P-type LaFeO3 Nanobelts by Electrospinning and Determination of Gas-Sensing Properties. *Sens. Actuators, B* **2011**, *153*, 83−88.

(47) Liu, K. W.; Shen, D. Z.; Shan, C. X.; Zhang, J. Y.; Jiang, D. Y.; Zhao, Y. M.; Yao, B.; Zhao, D. X. The Growth of ZnMgO Alloy Films for Deep Ultraviolet Detection. *J. Phys. D: Appl. Phys.* **2008**, *41*, 125104.

(48) Park, K. H.; Oh, S. J. Electron-Spectroscopy Study of Rare-Earth Trihalides. *Phys. Rev. B* **1993**, *48*, 14833−14842.

(49) Thirumalairajan, S.; Girija, K.; Hebalkar, N. Y.; Mangalaraj, D.; Viswanathan, C.; Ponpandian, N. Shape Evolution of Perovskite LaFeO3 Nanostructures: a Systematic Investigation of Growth Mechanism, Properties and Morphology Dependent Photocatalytic Activities. *RSC Adv.* **2013**, *3*, 7549−7561.

(50) Kersen, U. Microstructural And Surface Characterization of Solid State Sensor Based on LaFeO Oxide for Detection of NO. *Analyst* **2001**, *126*, 1377−1381.

(51) Hu, X.; Yu, J. C.; Gong, J.; Li, Q.; Li, G. α-Fe$_2$O$_3$ Nanorings Prepared by a Microwave-Assisted Hydrothermal Process and Their Sensing Properties. *Adv. Mater.* **2007**, *19*, 2324−2329.

(52) Hoa, N. D.; El-Safty, S. A. Synthesis of Mesoporous NiO Nanosheets for the Detection of Toxic NO$_2$ Gas. *Chem.—Eur. J.* **2011**, *17*, 12896−12901.

(53) Lu, R.; Zhou, W.; Shi, K.; Yang, Y.; Wang, L.; Pan, K.; Tian, C.; Ren, Z.; Fu, H. Alumina Decorated TiO2 Nanotubes with Ordered Mesoporous Walls as High Sensitivity NOx Gas Sensors at Room Temperature. *Nanoscale* **2013**, *5*, 8569−8576.

(54) Tang, W.; Wu, X.; Li, D.; Wang, Z.; Liu, G.; Liu, H.; Chen, Y. Oxalate Route for Promoting Activity of Manganese Oxide Catalysts in Total VOCs' Oxidation: Effect of Calcination Temperature and Preparation Method. *J. Mater. Chem. A* **2014**, *2*, 2544−2554.

(55) D'Arienzo, M.; Armelao, L.; Cacciamani, A.; Mari, C. M.; Polizzi, S.; Ruffo, R.; Scotti, R.; Testino, A.; Wahba, L.; Morazzoni, F. One-Step Preparation of SnO$_2$ and Pt-doped SnO$_2$ as Inverse Opal Thin Films for Gas Sensing. *Chem. Mater.* **2010**, *22*, 4083−4089.

(56) Schedin, F.; Geim, A. K.; Morozov, S. V.; Hill, E. W.; Blake, P.; Katsnelson, M. I.; Novoselov, K. S. Detection of Individual Gas Molecules Adsorbed on Graphene. *Nat. Mater.* **2007**, *6*, 652−655.

(57) Batzill, M.; Diebold, U. The Surface and Materials Science of Tin Oxide. *Prog. Surf. Sci.* **2005**, *79*, 47−154.

(58) Kim, H.-J.; Lee, J.-H. Highly Sensitive and Selective Gas Sensors Using P-Type Oxide Semiconductors: Overview. *Sens. Actuators, B* **2014**, *192*, 607−627.

(59) Jinkawa, T.; Sakai, G.; Tamaki, J.; Miura, N.; Yamazoe, N. Relationship between Ethanol Gas Sensitivity and Surface Catalytic Property of Tin Oxide Sensors Modified with Acidic or Basic Oxides. *J. Mol. Catal. A: Chem.* **2000**, *155*, 193−200.

(60) Kovalenko, V.; Zhukova, A.; Rumyantseva, M.; Gaskov, A.; Yushchenko, V.; Ivanova, I.; Pagnier, T. Surface Chemistry of Nanocrystalline SnO$_2$: Effect of Thermal Treatment and Additives. *Sens. Actuators, B* **2007**, *126*, 52−55.

(61) Hosseinpour, N.; Khodadadi, A. A.; Bahramian, A.; Mortazavi, Y. Asphaltene Adsorption onto Acidic/Basic Metal Oxide Nanoparticles toward In Situ Upgrading of Reservoir Oils by Nanotechnology. *Langmuir* **2013**, *29*, 14135−14146.

(62) Rumyantseva, M.; Kovalenko, V.; Gaskov, A.; Makshina, E.; Yuschenko, V.; Ivanova, I.; Ponzoni, A.; Faglia, G.; Comini, E. Nanocomposites SnO$_2$/Fe$_2$O$_3$: Sensor and Catalytic Properties. *Sens. Actuators, B* **2006**, *118*, 208−214.

(63) Zeng, W.; Liu, T.-M. Gas-Sensing Properties of SnO$_2$−TiO$_2$-Based Sensor for Volatile Organic Compound Gas and Its Sensing Mechanism. *Physica B* **2010**, *405*, 1345−1348.